Nanoscale Horizons

Accepted Manuscript

This article can be cited before page numbers have been issued, to do this please use: Z. Jiang, P. Wang, X. Jiang and J. Zhao, *Nanoscale Horiz.*, 2018, DOI: 10.1039/C7NH00197E.

ROYAL SOCIETY OF CHEMISTRY

rsc.li/nanoscale-horizons

ROYAL SOCIETY OF CHEMISTRY
View Article Online
DOI: 10.1039/C7NH00197E

Journal Name

COMMUNICATION

MBene (MnB): a new type of 2D metallic ferromagnet with high Curie temperature

Received 00th January 20xx,
Accepted 00th January 20xx

DOI: 10.1039/x0xx00000x

www.rsc.org/

Zhou Jiang, [a] Peng Wang, [a] Xue Jiang, [a*] and Jijun Zhao [a]

We extend the 2D MXenes family into boride world, namely, MBenes. High-throughput calculations screen twelve MBenes with excellent stability. Among them, 2D MnB MBene exhibits robust metallic ferromagnetism (~3.2 μ_B per Mn atom) and high Curie temperature (345 K). After functionalization with F- and OH-groups, the ferromagnetic ground state of 2D MnB is well preserved. The Curie temperature is enhanced to 405 and 600 K, respectively, providing a novel and feasible strategy to tailor the T_C of 2D magnetic materials.

Conceptual insights

MXenes exfoliated from the bulk MAX phases have emerged as promising 2D materials. Inspired by recently fabricated crystalline ternary borides (MAB phases), we extend the MXenes family into boride world, namely MBenes. From *ab initio* high-throughput search, we identify twelve stable MBene sheets that may exist in reality. Among them, MnB sheet exhibits robust metallic ferromagnetism and high Curie temperature, rendering promising candidate for spintronics. Remarkably, with the help of F- and OH- functional groups on the surface, the ferromagnetic ground state can be well preserved and the Curie temperature is even enhanced by up to 255 K. The thermal and mechanical stabilities of MnB sheet have been confirmed and its possible mechanical exfoliation from bulk ternary borides has also been assessed by ideal fracture strength. Once the predicted MnB and other MBene sheet sheets are synthesized, they would open a new avenue of 2D materials and devices.

1. Introduction

Graphene, owing to its flat structure and high surface area, holds great promise for applications in electronics, magnetics, optics, optoelectronics, thermoelectrics, catalyst, and energy storage systems.[1, 2] The boom of graphene has stimulated the discovery and fabrication of a wealth of other two-dimensional (2D) materials.[3] Transition metal carbides, nitrides and carbides/nitrides (namely, MXenes) are attractive additions to the 2D family. MXenes are mainly produced by selectively etching the atomic layers from their layered parents of bulk MAX phases. MAX phases are named after their compositions, where M is a transition metal, A is an element mostly in IIIA and IVA columns, and X is carbon or nitrogen.[4] So far, more than 70 MXenes have been theoretically predicted and 19 of them have been experimentally synthesized.[5] Applications of MXenes in field effect transistors,[6] Li ion batteries,[7] catalysts,[8] and photocatalyst[9] have been explored. Even with such a wide variety of MXenes, an intriguing question arises: whether X can be extended to the other elements?

Boron is the fifth element on the periodic table and its number of valence electrons is only one/two less than carbon/nitrogen. Its electron deficiency, electronegativity, and atomic size would endow 2D boron materials with distinctly different properties from the other 2D materials. For instance, most elementary 2D materials are the graphene analogues with flat or buckled honeycomb structures, while borophene has a triangular lattice with different arrangements of hexagonal holes.[10,11] The biggest challenge for synthesis of boron based 2D materials is surplus electron balance, which can be solved by hexagonal hole introduction[12,13] and metal substrate passivation[14,15]. Another practical method to realize the 2D boron based systems is the combination between boron and various transition metals. On one hand, the transition metal would donate electron to boron to stabilize the boron sheet. On the other hand, the highly coordinated transition metal center may endow novel complexity and diversity to 2D boride materials.

Among transition metal borides family, only magnesium diboride[16] and titanium diboride[17] sheets have been synthesized by exfoliation through ultrasonication and intercalation of alkali metals. However, the conventional chemical etching method to produce MXenes from the corresponding MAX phases has not been reported for 2D transition metal borides. This is mainly

[a] *Key Laboratory of Materials Modification by Laser, Ion and Electron Beams (Dalian University of Technology), Ministry of Education, Dalian 116024, China*
** corresponding authors: Email: jiangx@dlut.edu.cn, zhaojj@dlut.edu.cn*

†Electronic Supplementary Information (ESI) available: [Geometries, phonon band structures and other detail information for twelve MBenes (MnB, HfB, ZrB, Au_2B, Mo_2B, Nb_5B_2, Nb_3B_4, Ta_3B_4, V_3B_4, OsB_2, FeB_2, and RuB_2), AIMD simulation results, spin-polarized band structures (PBE and HSE06 methods), four magnetic configurations of MnB sheet and its functionalized structural forms (MnBF and MnBOH) with corresponding density of states.]. See DOI: 10.1039/x0xx00000x

limited by the lack of ternary borides having layered crystal structures with easily etching layers. Recently, MAX analogues, a series of single crystalline ternary borides (MAB phases) have been successfully fabricated, including Cr_2AlB_2, Cr_3AlB_4, Cr_4AlB_6, WAlB, MoAlB, Mn_2AlB_2, and Fe_2AlB_2.[18] These structures are composed of aluminium layers that are suitable to generate 2D transition metal borides, as demonstrated in the previous studies of MXenes.[4, 19-21] Since these 2D transition metal borides originate from the ternary borides, we name them as MBenes. If any of the MBenes can be verified in experiment, the rich of boron chemistry would open a new avenue with diverse applications. Then it is natural to ask: is it possible to obtain 2D MBenes from MAB phases?

To address this question, here we present *ab initio* high-throughput calculations to search for potential 2D MBenes candidates. From an analysis of the database of binary borometallic molecules, twelve 2D borides (MnB, HfB, ZrB, Au_2B, Mo_2B, Nb_5B_2, Nb_3B_4, Ta_3B_4, V_3B_4, OsB_2, FeB_2, and RuB_2) stand out for their satisfactory stability. Among them, 2D metal MnB MBene possesses robust ferromagnetism (FM). Remarkably, its metallic behavior, ferromagnetic state and high Curie temperature are well retained even after functionalization of F- or OH- groups. As the first attempt to extend MXenes into boride systems, our findings not only enrich the possible diversity of 2D materials in theory but also bring about new opportunities of spintronic applications.

2. Computational details

Our calculations were carried out using spin-polarized density functional theory (DFT) within the generalized gradient approximation (GGA)[22] as implemented in the Vienna *Ab initio* Simulation Package (VASP),[23,24] with the Perdew-Burke-Ernzerhof (PBE) exchange-correlation functional. The projected augmented wave (PAW) approach was used to describe the ion-electron interaction.[25,26] To appropriately account for the strongly correlated electrons, GGA+U method was used to deal with the partially filled *d* orbitals of Mn atoms.[27] For the Mn 3*d*-orbitals, the effective on-site Coulomb interaction parameter (U) and the exchange interaction parameter (J) are set to be 3 eV and 1 eV, respectively. The choice of U and J values has been carefully tested by optimizing the lattice parameters of Mn_2AlB_2 and Mn_4B_4, and the results are given in Table S1. The energy cutoff of plane-wave basis was 650 eV. During geometry optimization, numerical convergence was achieved with the tolerance of 10^{-6} eV in energy and 0.001 eV/Å in force, respectively. To avoid interaction between a layer and its replica, a large vacuum space of 16 Å was added along the **z** axis. The Brollouin zone was sampled with a 19×19×1 Monkhorst-Pack *k*-points grid for geometry optimization and a set of 23×23×1 grid for electronic structure calculations, respectively. For the equilibrium MBene structures, their phonon dispersions were computed using the direct supercell method as implemented in the Phonopy program.[28] *Ab initio* molecular dynamics (AIMD) simulations were also performed to assess the thermal stability of 2D MnB structure and its functionalization form (MnBF and MnBOH) at 600 K, 900 K and 1200 K, respectively.

3. Results and discussion

A high-throughput structural search was carried out to identify the stable structures of 2D transition metal borides M*x*B*y*, where M stands for transition metals in 3*d* (Ti, V, Cr, Mn, Fe, Co, Ni, Cu and Zn), 4*d* (Zr, Nb, Mo, Tc, Ru, Rh, Pd, Ag and Cd) and 5*d* (Hf, Ta, W, Re, Os, Ir, Pt, Au and Hg), and the ratios of *x*:*y* are 1:2, 3:4, 1:1, 2:1, and 5:2. Among them, we identified twelve unprecedented 2D MBenes, including MnB, HfB, ZrB, Au_2B, Mo_2B, Nb_5B_2, Nb_3B_4, Ta_3B_4, V_3B_4, OsB_2, FeB_2, and RuB_2. Their crystalline structures are displayed in Fig. S1(a). The cohesive energies, bond lengths, and slice thicknesses are listed in Table S2. The cohesive energy is defined as

$$E_{coh} = (xE_M+yE_B-E_{MxBy})/(x+y),$$

where E_M, E_B are the total energies of an isolated transition metal and B atom, respectively; E_{MxBy} is the total energy of the unit cell of the TMB sheet. The average value of these cohesive energies are 6.08 eV/atom, which is comparable to the common 2D layered materials like MoS_2 (5.02 eV/atom), $g_{1/8}$ borophene sheet (5.81 eV/atom) and Mo_2C (5.98 eV/atom). Their dynamic stability was further assessed in terms of phonon band structure (Fig. S1(b)), and no imaginary frequencies were observed throughout the entire Brillouin zone. Both satisfactory cohesive energy and phonon dispersion imply that those 2D MBenes candidates are thermodynamically and dynamically stable. Among these twelve systems, 2D MnB MBene possesses the largest magnetic moments (Table S1), which arouse our interests to explore its other properties further.

Fig. 1(a) presents the optimized structure of 2D MnB sheet. Its unit cell with lattice constants of a = 2.881 Å and b = 2.932 Å contains two Mn atoms and two B atoms. Unlike the common hexagonal 2D materials such as graphene,[29] silicene[30] MoS_2[31] and Ti_3C_2[20], the 2D MnB sheet shows a rectangular lattice with space group of *Pmma* (No. 51), leading to anisotropy in the *x* and *y* directions. Each Mn or B atom form six bonds with its neighbouring atoms, with a bilayer buckled structure with Mn atoms on the upmost surfaces and the distance between Mn layers being h=2.125 Å. The intralayer Mn-B bond length is 2.119 Å (d_1) and the interlayer one is 2.176 Å (d_2).Due to the electron deficiency of boron, the Mn-B bond in MnB is slightly weaker than those in the Mn_2C[32] and MnN_2[33] where the Mn-C and Mn-N bond lengths are 1.956 and 1.949 Å, respectively. Note that, in the database of binary boron compounds,[34] such borides with one dimensional zigzag chains have also been observed in the bulk MnB, CrB, and MoB crystals. Our proposed 2D MnB is different from them by the relative position of parallel zigzag chains forming by Mn atoms. This unique configuration suggests the MnB sheet with distinct physical and chemical properties.

The calculated cohesive energy of sheet MnB sheet is 4.80 eV/atom, which is slightly lower than that of bulk MnB crystal (5.35 eV) and higher than the recently proposed Mn-containing MXenes phases such as Mn_2C (4.42 eV/atom) and MnN_2 (3.45

View Article Online
DOI: 10.1039/C7NH00197E

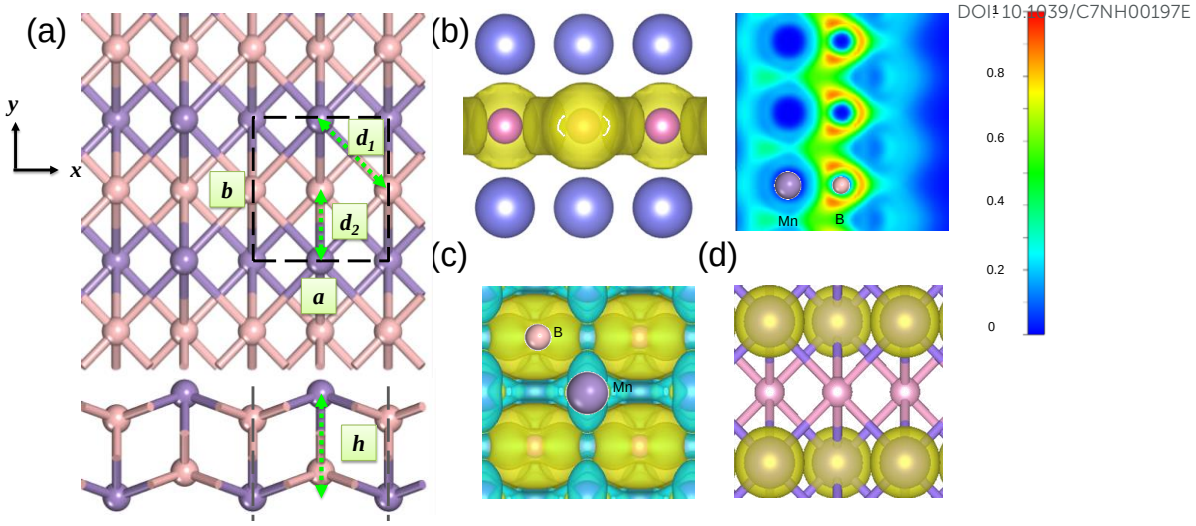

Fig. 1 (a) Top and side view of a 2D MnB sheet, ***a*** and ***b*** is the lattice parameters, and ***h*** denotes the thickness of the layer. (b) Maps of the electron localization function (ELF) located (0 –1 –6) plane with a scale bar from 0 to 1. (c) The deformation density of MnB sheet with an isosurface of 0.01 e Å^{-3}. The yellow and cyan region represents the accumulation and depletion of the electron, respectively. (d) The spin polarization distribution with an isosurface of 0.75. The yellow color indicates a net spin-up polarization, and the spin polarization is mainly on the Mn sites.

eV/atom). From our calculations, the 2D elastic constants of C_{11}, C_{12}, C_{22}, and C_{44} are 197, 50, 158 and 90 N/m, respectively, satisfying the Born-Huang stability criteria[35] and confirming that MnB layer is mechanically stable. To further check its thermal stability, we used a relatively large 4×4 supercell to carry out AIMD simulations within the canonical ensemble (NVT) at temperatures of 300, 600, and 1200 K, respectively. Up to 1200 K, no severe geometrical reconstructions are observed after 20 ps (Fig. S2 (a)) and the average displacement of Mn atoms is about 0.08 Å, which means that the framework of Mn atoms basically remains unchanged.

To explain the origin of high stability and gain a deep insight into the bonding characters, we calculated the electron localization function (ELF). The homogeneous electron gas is renormalized to the values from 0.0 to 1.0 in difference colours. By definition, the region with a value of 1.0 indicates perfect electron localization, 0.5 represents a fully delocalized electron, and the region with the value close to 0.0 refers to very low charge density.[22] From Fig. 1 (b), one can clearly see that ELF for the region around Mn atoms is 0.0, indicating their electron deficiency. At the same time, the B frameworks are fully surrounded by homogeneous electron gas (ELF = 0.5), which is crucial to stabilize the entire 2D sheet via strong B-B bonds. Bader charge analysis shows that each Mn atom donates approximately 0.68 electrons to each B atom within MnB sheet, reflecting nature of Mn-B ionic bonding. This can be understood by the electronegativities of B (2.04) and Mn (1.55). The electron transfer from Mn to B further contributes to the high stability of 2D MnB system. As shown in Fig. 1(c), the deformation electronic density (DED) also verifies the above bonding characteristics. The transferred electrons are mostly accumulated around the B sites, in agreement with the ELF analysis.

Considering its high stability, it is natural to wonder how the MnB sheet can be synthesized in experiments. There are three feasible pathways to support our hypothetical 2D MnB sheet. Firstly, the Mo_2C MXene was prepared with the traditional chemical vapour deposition (CVD) method,[36] which is commonly used for growing graphene, MoS_2, and many other 2D materials. Thus, monolayer transition borides might also be fabricated using CVD growth. Secondly, the ternary layered phases Mn_2AlB_2 has already been synthesized by arc-melting.[18] The corresponding MnB sheet can be produced by selective chemical etching of Al metal layer. Such method has been successfully employed to convert 3D MAX phases (Ti_2AlC, Nb_2AlC, V_2AlC, and $(Ti_{0.5}Nb_{0.5})AlC$ to 2D MXene phases of Ti_2C, Nb_2C, V_2C, and $(Ti_{0.5}Nb_{0.5})C$, respectively.[19] Thirdly, one can also attempt to mechanically exfoliate MBenes from MAB phases. For further confirm the possibility, we have investigated the tensile deformation mechanism of Mn_2AlB_2. Both the stress-strain curves and ELF counter plots (Fig. 2) show that when the tensile strain increases from 1% to 30% along the *z* axis, the strength of B-Mn bonds remain unchanged, while the Mn-Al bonds are significantly weakened as electrons are localized around Al atoms. This implies that the MnB layers are likely to be separated from the Al layers via Mn-Al bond breaking. In addition, the ideal fracture strength for mechanical exfoliation is as low as 32 GPa, which is comparable to the values of W_2AlC (36 GPa), Cr_2AlC (35 GPa), Mo_2AlC (34 GPa), Ta_2AlC (32 GPa), and V_2AlC (32 GPa)[37]. This implies that mechanically exfoliating MnB layers from Mn_2AlB_2 crystal is feasible.

The spin-polarized band structures in Fig. S3 show that the MnB sheet is metallic with several partially occupied bands crossing the Fermi level in both spin channels. The metallicity is further confirmed by the result of computations using HSE06 functional.[38] Moreover, the atom-projected and orbit-projected

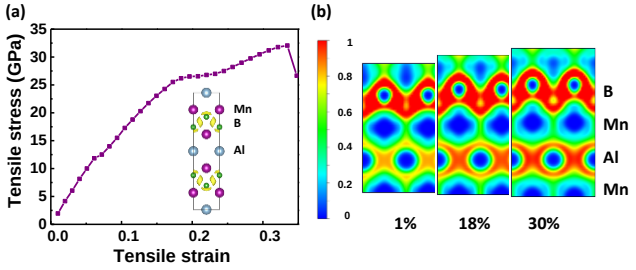

Fig. 2 (a) The calculated stress-strain curve of Mn_2AlB_2 with the ELF contour plots and (b) projected on the plane containing Mn and Al atoms under the [0001] tensile strains of 1%, 18%, and 30%.

Table 1 Atomic charge differences (electron per atom) from Bader charge analysis (positive and negative values indicate electron gain and loss, respectively), the atomic and orbital magnetic moments M of MnB, MnBX (X=F or OH). M_T represents the total magnetic moment.

system	Q_{Mn} / e	Q_B / e	Q_X / e	M_{Mn} / μ_B	$M_{Mn\text{-}d}$ / μ_B	M_B / μ_B	$M_{B\text{-}p}$ / μ_B	M_X / μ_B	M_T / μ_B
MnB	–0.68	0.68	--	3.20	3.15	–0.18	–0.15	--	6.04
MnBF	–1.10	0.51	0.59	3.24	3.20	–0.20	–0.16	0.06	6.20
MnBOH	–1.10	0.50	0.60	3.15	3.11	–0.20	–0.16	0.07	6.04

bands in Fig. 3 demonstrate that the metallicity is derived from Mn-3*d* orbitals (Mn-d_{xy}, $d_{x^2-y^2}$, d_{xz}) and B-*p* orbitals near the Fermi energy. As listed in Table 1, the total magnetic moment of 6.04 μ_B per unit cell is mainly contributed by Mn atoms, which is intuitively shown in the spin-density distribution in Fig. 1(d). Each Mn atom has an on-site moment of 3.2 μ_B and the spin moments of boron atoms (–0.18 μ_B) align antiferromagnetically. To further clarify the origin of magnetic moments, Fig. 4 shows the atom-projected and Mn-3*d* orbital-projected density of states. It is clear that Mn-3*d* (d_{yz}, d_{xz}, $d_{x^2-y^2}$) are fully occupied in spin-up states, while the d_{xy} and d_{z^2} are partially filled in both up and down spin channels. Mn's five *d* orbitals are in non-degenerate energies, which originate from the B induced asymmetric octahedral crystal field around Mn atoms. The strong hybridization between B-*p* orbitals and Mn-*d* orbitals are responsible for such phenomenon. Hence, its electronic structure can be expected for a formal Mn^{3+} electronic configuration in high spin state with three unpaired *d* electrons ($d^{3\uparrow}$ spin configuration). The atom and orbit-projected electronic band structure analysis (Fig. 3) also confirm the *p*-*d* hybridization and the difference of the dispersions in the two spin channels associated with the crystal field splitting.

In order to further explore the preferred magnetic interaction, we optimized a 2×2 MnB supercell and considered four possible magnetic configurations (Fig. S4): one ferromagnetic (FM) and three antiferromagnetic (AFM). The exchange energy is defined as $E_{ex} = (E_{AFM}\text{-}E_{FM})$ per Mn_8B_8 formula, where E_{AFM} and E_{FM} are the energies of the Mn atoms with AFM and FM coupling in the 2×2 MnB sheet. The calculated energy differences between these magnetic

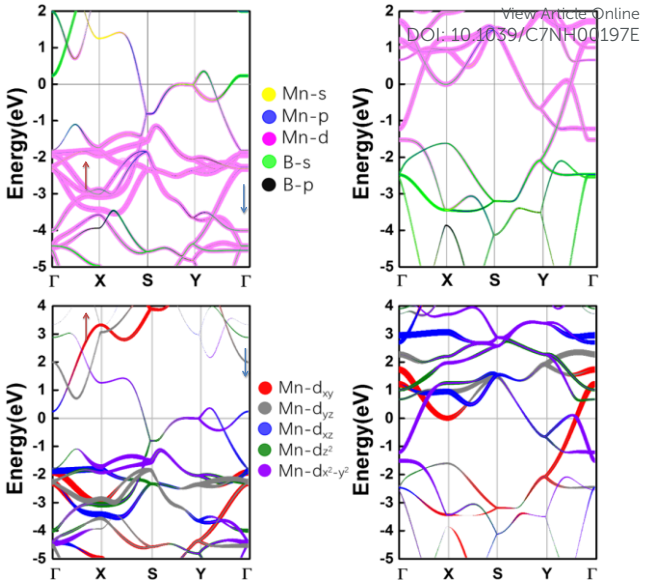

Fig. 3 Atom-projected and orbital-projected band structures of MnB sheet in spin-up and spin-down channels, and the Fermi levels are set to zero.

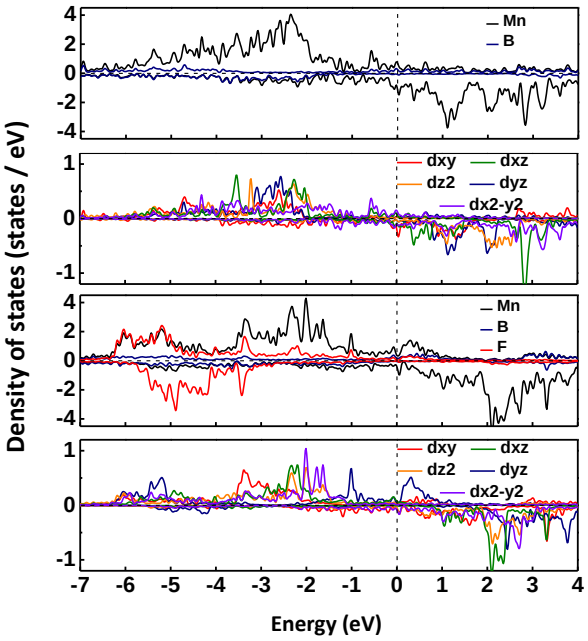

Fig. 4 Atom-projected and orbital-projected density of states for MnB and MnBF sheets and the Fermi levels are all set to zero.

configurations are summarized in Table 2. For the MnB sheet, the FM ground state is more stable than the AFM ones by at least 180 meV per Mn_8B_8 formula. As discussed above, the indirect *p*-*d* exchange interaction plays an important role in the ferromagnetic coupling of MnB sheet.

One important quantity of ferromagnetism is the Curie temperature (T_C) corresponding to the transition from ferromagnetic to paramagnetic phase. For practical spintronic applications, T_C above room temperature is desirable. Here T_C is estimated using 2D Heisenberg model, where the Hamiltonian operator can be written as

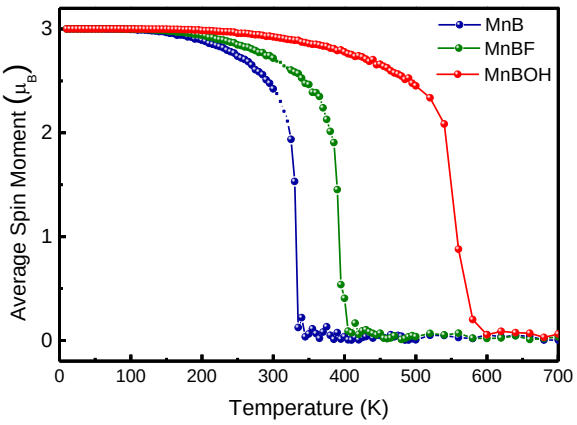

Fig. 5 On-site magnetic moment of Mn atom versus temperature in MnB (blue), MnBF (green), MnBOH (red) sheets.

Table 2 Calculations energy of ferromagnetic state (E_{FM}) and antiferromagnetic states (E_{AFM}), the energy differences (ΔE) between E_{AFM} and E_{FM} for Mn_8B_8 formula and the magnetic moments (M_{total}) of each states

	E_{Total} / eV	ΔE / meV	M_{total} / μ_B
FM	–108.697	0	25.46
AFM1	–108.198	499	0
AFM2	–108.218	479	0
AFM3	–108.517	180	0

$$H = -\Sigma_{i,j} J_1 M_i M_j - \Sigma_{k,l} J_2 M_k M_l - \Sigma_{p,q} J_3 M_p M_q,$$

where M_i is the magnetic moment at site I; J is the exchange coupling parameters: J_1, J_2 and J_3 stand for the nearest, second-nearest, and third-nearest site pairs. From the distance between nearest, second-nearest, and third-nearest Mn atoms of 2.567, 2.881 and 2.932 Å, respectively, the calculated exchange coupling parameters J_1, J_2 and J_3 are 3.1, 1.4 and -2.3 meV (Details is in ESI S4). Within mean field approximation (MFT), the estimated T_C is in the range of 258~418 K. It is known that MFT cannot accurately describe the magnetic percolation effect and tends to overestimate T_C. Therefore, we evaluated T_C of the MnB sheet by using Monte Carlo (MC) simulation based on 2D Ising model of 100×100 supercell, and the simulation lasted for 1.2×10^5 iterations. The temperature-dependent magnetic moment for the MnB sheet is plotted in Fig. 5, showing that the magnetic moment falls drastically at temperature of $T_C \sim 345$ K. Compared with the above estimation with MFT, T_C is reduced by 17%. Even so, it is still higher than room temperature and those of many previously reported 2D magnetic materials such FeC_2 (245 K),[39] MnO_2 (140 K),[40] Cr@gt-C_3N_3 (325 K),[41] MnPc (150 K)[42] and Nb_3Cl_8 (31 K).[43] Moreover, the T_C value for MnB is significantly higher than the highest T_C value (110 K) achieved experimentally in Mn-doped GaAs monolayer.[44]

The magnetic anisotropy energy (MAE) is an important property for high density storage and quantum spin processing. In principle, reducing dimensionality and symmetry would increase MAE relative to the corresponding 3D bulk phase. For MnB sheet, the easy magnetization axis is *z* direction (out-of-plane), along which the magnetization energy is lower than that along the x- and y-direction by 25 and 175 μeV per Mn atom, respectively. These MAE values are comparable to reported 2D material Mn_2C (25 μeV),[32] and bulk Co (65 μeV per Co atom), and is one order of magnitude higher than bulk Fe (1.4 μeV /atom) and Ni (2.7 μeV /atom).[45] The sizeable MAEs endow the MnB sheet potentially useful for magnetoelectronics applications.

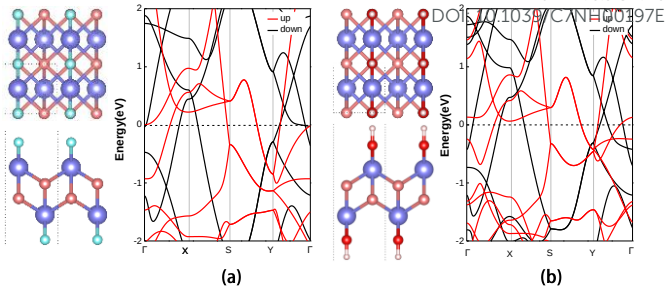

Fig. 6 (a) and (b) are the side and top views of MnBX (X= F or OH) structural forms and the corresponding spin-polarized band structure.

Considering that bare MnB sheet is chemically active and could be exfoliated and terminated with F- and OH- groups in experiment,[19] we further exploit the influence of these functional groups on the structural, electronic and magnetic properties of MnB sheet. As representatives, we considered two functionalized species, i.e., MnBF and MnB(OH). As shown in Fig. S5, three possible configurations are considered for each MnB sheet, where the functional groups are placed at the top site of B atoms (H_1), hollow sites of Mn atoms (H_2), and hollow sites of B atoms (H_3). We find that both OH/F- functional groups are most energetically favorable at the hollow site B atoms (H_3) on both sides. This is understandable since the Mn atoms are the electron donor and the functional groups are more likely to bond with Mn atoms than B atoms. Indeed, a significant electron transfer (Table 1) from Mn-3*d* orbital to F- and OH- functional groups has been observed in MnBF and MnB(OH) by 0.59 e and 0.60 e, respectively, in addition to the electron transfer from Mn to B by 0.5 e in average, whereas no electron transfer was seen between B atom and F-, and OH-functional groups. As a consequence, such charge transfer slightly elongated the Mn-B bonds, that is, the average Mn-B bond lengths of OH-terminated and F-terminated MnB sheet are 2.223 Å, and 2.239 Å, respectively. Our AIMD simulations of MnBF and MnBOH indicate that both of them are thermal stable at 600K after 20 ps (Fig. S2 (b)).

We further investigated the electronic and magnetic properties of those functionalized MnB. Both MnB derivatives still exhibit metallic behavior, as clearly seem from the spin-polarized electronic band structures in Fig. 6. More importantly, the magnetic ground state and magnetic moments on the Mn atoms are well retained after functionalization (Table 1). For MnBF and MnB(OH), the FM state is more stable than AFM state by 340 meV and 77 meV per 2×2

View Article Online
DOI: 10.1039/C7NH00197H

Table 3 The comparison of magnetic moments (*M*), energy differences (ΔE for 2× 2 supercell), and T_C using MFA and MC for MnB, MnBX (X = F or OH), respectively.

	M_T / μ_B	M_{Mn} / μ_B	ΔE /meV	T_C(MFA) / K	T_C(MC) / K
MnB	6.04	3.20	180	217-347	345
MnBF	6.20	3.24	340	618-989	405
MnBOH	6.04	3.15	77	333-532	600

supercell, respectively (Table 3). At the same time, the on-site magnetic moments on Mn atoms are 3.20, 3.24, and 3.15 μ_B for MnB, MnBF, and MnB(OH), respectively. Total and orbital-projected density of states of MnB and MnBF sheets in Fig. 4. The almost unchanged magnetic behavior is closely related to the highly split *d* orbitals of Mn atoms. Initially the d_{yz} orbitals in the spin-up channel are occupied, while the dx^2-y^2 orbitals partially occupy the spin-down channel. Upon functionalization, the d_{yz} orbitals in the spin-up channel change to partially occupied, while the dx^2-y^2 in the spin-up channel becomes fully occupied. This results in the robust magnetic moment of ~3μ_B per Mn atom for both MnB and MnBF sheets. A similar picture is applicable to the case of the MnBOH system, and the PDOS is shown in Fig. S6.

The Curie temperatures of MnBF and MnBOH sheets are then estimated by MFA method and MC simulation, and the results are listed in Table 1. Fig. 5 shows that the T_C is further increased up to 405 K (MC) and 600 K (MC) through F- and OH- functionalization. Note that this value is also comparable to the calculated high T_C of a functionalized Mn-based 2D system, i.e., Mn_2CF_2 (520 K).[46] The insensitive metallic behavior, robust FM state and high Curie temperature of MnB sheet is superior to most reported 2D MXene materials.[47] Taking Ti_2C as an example, the magnetic moment of Ti_2C is 0.982 μ_B /atom. However, upon functionalization, the magnetism is quenched, which strongly limit their practical application in spintronics. More excitingly, our results suggest that chemical functionalization is an effective method to tailor T_C for 2D magnetic materials. In present situation, the Curie temperatures of MnBF, and MnB(OH) are 60 and 255 K higher than the pristine MnB sheet.

Conclusions

In summary, motivated by the recent experimentally obtained 3D MAB phases, we explored the geometrical, electronic, and magnetic properties of their 2D MBene analogues. Taking MnB as an example, exfoliation from 3D crystal to 2D layer is feasible, as confirmed by their low fracture strength, high thermal, dynamical, and mechanical stabilities. The 2D MnB MBene sheet as well as its functionalized products exhibit metallic ferromagnetic behavior with the Curie temperature above room temperature (345-600 K). The ferromagnetism and metallicity are mainly arising from *p-d* hybridization mechanism and crystal field splitting. Importantly, the characteristic of the high temperature ferromagnetic metal is insensitive to their chemical functionalization. These advantages endow 2D MnB MBene a promising material for the spintronic devices. Like MXene, the transition metal borides can lead to many possible 2D binary compounds, e.g., MnB, HfB, ZrB, Au_2B, Mo_2B, Nb_5B_2, Nb_3B_4, Ta_3B_4, V_3B_4, OsB_2, FeB_2, and RuB_2 sheets are predicted as potential metastable phases. Their fruitful applications will be reported in our future study. Our first successful attempt to extend the MXenes into boride systems would significantly promote the diversity of 2D materials and encourage scientists to design and synthesize those interesting 2D MBene materials in the future.

Conflicts of interest

There are no conflicts to declare

Acknowledgements

This work is supported by the National Natural Science Foundation of China (11404050, 11574040) and the Fundamental Research Funds for the Central Universities of China (DUT16RC(4)50, DUT16JJ(G)05, DUT16LAB01, DUT17LAB19). We also acknowledge the Supercomputing Center of Dalian University of Technology for providing the computing resource.

Notes and references

1. J. Pan, S. Lany and Y. Qi, *ACS Nano*, 2017, **11**, 7560-7564.
2. M. Khazaei, A. Ranjbar, M. Arai, T. Sasaki and S. Yunoki, *J. Mater. Chem. C*, 2017, **5**, 2488-2503.
3. S. Z. Butler, S. M. Hollen, L. Cao, Y. Cui, J. A. Gupta, H. R. Gutierrez, T. F. Heinz, S. S. Hong, J. Huang, A. F. Ismach, E. Johnston-Halperin, M. Kuno, V. V. Plashnitsa, R. D. Robinson, R. S. Ruoff, S. Salahuddin, J. Shan, L. Shi, M. G. Spencer, M. Terrones, W. Windl and J. E. Goldberger, *ACS Nano*, 2013, **7**, 2898-2926.
4. M. Naguib, O. Mashtalir, J. Carle, V. Presser, J. Lu, L. Hultman, Y. Gogotsi and M. W. Barsoum, *ACS Nano*, 2012, **6**, 1322.
5. B. Anasori, M. R. Lukatskaya and Y. Gogotsi, *Nat. Rev. Mater.*, 2017, **2**, 16098.
6. S. Lai, J. Jeon, S. K. Jang, J. Xu, Y. J. Choi, J. H. Park, E. Hwang and S. Lee, *Nanoscale*, 2016, **8**, 1216.
7. Q. Tang, Z. Zhou and P. Shen, *J. Am. Chem. Soc*, 2012, **134**, 16909-16916.
8. G. Fan, X. Li, Y. Ma, Y. Zhang, J. Wu, B. Xu, T. Sun, D. Gao and J. Bi, *New J. Chem.*, 2017, **41**, 2793-2799.
9. Z. Guo, J. Zhou, L. Zhu and Z. Sun, *J. Mater. Chem. A*, 2016, **4**, 11446-11452.
10. A. J. Mannix, X. F. Zhou, B. Kiraly, J. D. Wood, D. Alducin, B. D. Myers, X. Liu, B. L. Fisher, U. Santiago, J. R. Guest, M. J. Yacaman, A. Ponce, A. R. Oganov, M. C. Hersam and N. P. Guisinger, *Science*, 2015, **350**, 1513-1516.

11. B. Feng, J. Zhang, Q. Zhong, W. Li, S. Li, H. Li, P. Cheng, S. Meng, L. Chen and K. Wu, *Nat. Chem.*, 2016, **8**, 563-568.
12. H. Tang and S. Ismail-Beigi, *Phys. Rev. Lett.*, 2007, **99**, 115501.
13. X. Wu, J. Dai, Y. Zhao, Z. Zhuo, J. Yang and X. C. Zeng, *ACS Nano*, 2012, **6**, 7443-7453.
14. Y. Liu, E. S. Penev and B. I. Yakobson, *Angew. Chem., Int. Ed. Engl.*, 2013, **52**, 3156-3159.
15. H. Liu, J. Gao and J. Zhao, *Sci. Rep.*, 2013, **3**, 3238.
16. C. Cepek, R. Macovez, M. Sancrotti, L. Petaccia, R. Larciprete, S. Lizzit and A. Goldoni, *Appl. Phys. Lett.*, 2004, **85**, 976-978.
17. G. Hilz and H. Holleck, *Int. J. Refract. Met. Hard Mater.* , 1996, **14**, 97-104.
18. P. Chai, S. A. Stoian, X. Tan, P. A. Dube and M. Shatruk, *J. Solid State Chem.*, 2015, **224**, 52-61.
19. M. Naguib, V. N. Mochalin, M. W. Barsoum and Y. Gogotsi, *Adv. Mater.*, 2014, **26**, 992-1005.
20. M. Naguib, M. Kurtoglu, V. Presser, J. Lu, J. Niu, M. Heon, L. Hultman, Y. Gogotsi and M. W. Barsoum, *Adv. Mater.*, 2011, **23**, 4248-4253.
21. M. Ghidiu, M. Naguib, C. Shi, O. Mashtalir, L. M. Pan, B. Zhang, J. Yang, Y. Gogotsi, S. J. Billinge and M. W. Barsoum, *Chem. Commun.*, 2014, **50**, 9517-9520.
22. J. P. Perdew, K. Burke and M. Ernzerhof, *Phys. Rev. Lett.*, 1997, **77**, 3865.
23. G. Kresse and J. Furthmuller, *Phys. Rev. B.*, 1996, **54**, 11169-11186.
24. G. Kresse and J. Furthmuller, *Comput. Mater. Sci.*, 1996, **6**, 15-50.
25. P. E. Blöchl, *Phys. Rev. B.*, 1994, **50**, 17953-17979.
26. G. Kresse and D. Joubert, *Phys. Rev. B.*, 1999, **59**, 1758-1775.
27. A. I. Liechtenstein, V. I. Anisimov and J. Zaanen, *Phys. Rev. B.*, 1995, **52**, R5467-R5470.
28. K. Parlinski, Z. Q. Li and Y. Kawazoe, *Phys. Rev. Lett.*, 1997, **78**, 4063-4066.
29. K. S. Novoselov, D. Jiang, F. Schedin, T. J. Booth, V. V. Khotkevich, S. V. Morozov and A. K. Geim, *Proc. Natl. Acad. Sci. USA*, 2005, **102**, 10451-10453.
30. J. Zhao, H. Liu, Z. Yu, R. Quhe, S. Zhou, Y. Wang, C. C. Liu, H. Zhong, N. Han, J. Lu, Y. Yao and K. Wu, *Prog. Mater Sci.*, 2016, **83**, 24-151.
31. H. Shu, F. Li, C. Hu, P. Liang, D. Cao and X. Chen, *Nanoscale*, 2016, **8**, 2918-2926.
32. L. Hu, X. Wu and J. Yang, *Nanoscale*, 2016, **8**, 12939-12945.
33. J. Liu, Z. Liu, T. Song and X. Cui, *J. Mater. Chem. C*, 2017, **5**, 727-732.
34. G. Akopov, M. T. Yeung and R. B. Kaner, *Adv. Mater.*, 2017, **29**.
35. M. Born, K. Huang and M. Lax, *Am. J. Phys.*, 1954, **39**, 113-127.
36. C. Xu, L. Wang, Z. Liu, L. Chen, J. Guo, N. Kang, X. L. Ma, H. M. Cheng and W. Ren, *Nat. Mater.*, 2015, **14**, 1135-1141.
37. Z. Guo, L. Zhu, J. Zhou and Z. Sun, *RSC Adv.*, 2015, **5**, 25403-25408.
38. J. Heyd, G. E. Scuseria and M. Ernzerhof, *J. Chem. Phys.*, 2003, **118**, 8207-8215.
39. T. Zhao, J. Zhou, Q. Wang, Y. Kawazoe and P. Jena, *ACS Appl. Mater. Interfaces*, 2016, **8**, 26207-26212.
40. M. Kan, J. Zhou, Q. Sun, Y. Kawazoe and P. Jena, *J. Phys. Chem. Lett.*, 2013, **4**, 3382-3386.
41. I. Choudhuri, P. Garg and B. Pathak, *J. Mater. Chem. C*, 2016, **4**, 8253-8262.
42. J. Zhou and Q. Sun, *J. Am. Chem. Soc*, 2011, **133**, 15113-15119.
43. J. Jiang, Q. Liang, R. Meng, Q. Yang, C. Tan, X. Sun and X. Chen, *Nanoscale*, 2017, **9**, 2992-3001.
44. F. Matsukura, H. Ohno, A. Shen and Y. Sugawara, *Phys. Rev. B.*, 1998, **57**, R2037-R2040.
45. G. H. O. Daalderop, P. J. Kelly and M. F. H. Schuurmans, *Phys. Rev. B.*, 1990, **41**, 11919-11937.
46. J. He, P. Lyu and P. Nachtigall, *J. Mater. Chem. C*, 2016, **4**, 11143-11149.
47. Y. Xie and P. R. C. Kent, *Phys. Rev. B.*, 2013, **87**.